Earth and Planetary Science Letters 415 (2015) 67–79

Contents lists available at ScienceDirect

Earth and Planetary Science Letters

www.elsevier.com/locate/epsl

Structure of the Central Altyn Tagh Fault revealed by magnetotelluric data: New insights into the structure of the northern margin of the India–Asia collision

Letian Zhang [a,b], Martyn Unsworth [c], Sheng Jin [a,b,*], Wenbo Wei [a,b], Gaofeng Ye [a,b], Alan G. Jones [d], Jianen Jing [a,b], Hao Dong [a,b], Chengliang Xie [a,b], Florian Le Pape [d], Jan Vozar [d]

[a] School of Geophysics and Information Technology, China University of Geosciences, Beijing 100083, China
[b] Key Laboratory of Geo-detection of Ministry of Education, Beijing 100083, China
[c] Department of Physics, University of Alberta, Edmonton, Alberta, Canada
[d] Dublin Institute for Advanced Studies, Dublin, Ireland

ARTICLE INFO

Article history:
Received 26 July 2014
Received in revised form 22 January 2015
Accepted 22 January 2015
Available online xxxx
Editor: A. Yin

Keywords:
northern margin of the Tibetan Plateau
Altyn Tagh Fault
2-D inversion
3-D inversion
lithospheric electrical structure
magnetotellurics

ABSTRACT

The Altyn Tagh Fault (ATF) is a left-lateral, strike-slip fault that forms the northern margin of the Tibetan Plateau and plays a significant role in accommodating the convergence between the colliding Indian and Eurasian plates. As a part of the fourth phase of the INDEPTH project, magnetotelluric (MT) data were collected across the central segment of the ATF to determine the lithospheric-scale structure of the fault system. Dimensionality analyses demonstrated that the MT data can be interpreted using two-dimensional approaches, but some localized 3-D effects are seen. Consequently, both 2-D and 3-D inversions were carried out, and a joint interpretation was made on the basis of these two types of models. Inversion models revealed two major conductors beneath the Qaidam Basin (QB) and Altyn Tagh Range (ATR), respectively. The conductive region beneath the QB was interpreted as a ductile layer in the lower crust to upper mantle that might represent flow beneath the western margin of the QB, whereas the large scale south-dipping conductor beneath the ATR is interpreted as a region with high fluid content formed by metamorphism associated with the oblique underthrusting of the Tarim Block beneath the northern Tibetan Plateau. These fluids migrate upwards through the fault system and have formed serpentinized zones in the crust. Combining these interpretations, a structural model compatible with diverse geophysical observations is proposed, in which we suggest the competing end-member rigid block model and continuum model are reconcilable with the continuum model locally dominant for the study region, as evidenced by a thickened crust.

1. Introduction

The ongoing continent–continent collision between the Indian and Eurasian plates has created the spectacular topography of the Tibetan Plateau over the last 50 Myr. The tectonic processes that occurred and are still occurring during this orogeny are still not fully understood and a wide variety of models have been proposed to explain the dynamics of this region (Tapponnier et al., 2001; Tilmann et al., 2003; Yin and Harrison, 2000). Horizontal crustal motion is clearly important, as evidenced by the major strike faults that characterize the Northern and Eastern parts of the plateau (Tapponnier et al., 2001). However, the contribution of horizontal motion on these faults to the overall mass balance of the orogen remains unresolved. Another important tectonic process that may be active is crustal flow (Clark and Royden, 2000; Royden et al., 1997), a process first proposed by Nelson et al. (1996).

The magnetotelluric MT method is a useful tool in studies of continental dynamics because it images subsurface electrical resistivity, which is a rock property sensitive to the presence of fluids and temperature, and can give important constraints on crustal rheology (Pommier et al., 2013). MT data have been used effectively in previous studies to reveal rheological properties associated with active tectonics, including studies of large-scale strike-slip faults such as the San Andreas Fault

* Corresponding author at: School of Geophysics and Information Technology, China University of Geosciences, Beijing 100083, China.
E-mail address: jinsheng@cugb.edu.cn (S. Jin).

http://dx.doi.org/10.1016/j.epsl.2015.01.025
0012-821X/

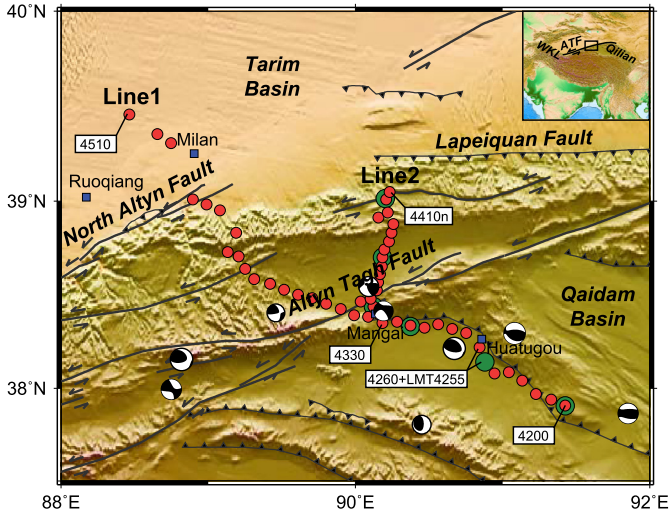

Fig. 1. Topography map showing major tectonic structures and MT station locations in the survey area. Red dots are broadband MT stations, green dots are long-period MT stations, blue squares are cities or towns, and texts in white boxes are station numbers. Figure was generated from GTOPO30 digital elevation data set using GMT (Wessel and Smith, 1995). Fault locations are taken from the HimaTibetMap-1.0 database (Styron et al., 2010). Focal mechanism solutions are from the Global Centroid Moment Tensor (CMT) Project (http://www.globalcmt.org). Abbreviations are: WKL, West Kunlun.; ATF, Altyn Tagh Fault.

(Becken et al., 2011; Unsworth and Bedrosian, 2004), the Alpine Fault (Wannamaker et al., 2002) and East Anatolian Fault (Türkoğlu et al., 2015). MT has played a major role in previous studies of the Tibetan Plateau (Bai et al., 2010; Unsworth et al., 2005; Wei et al., 2001). One key result from the MT studies is the observation of a low resistivity crustal layer along the southern and eastern margins of the Tibetan Plateau, where the resistivity values are consistent with crustal viscosities low enough to permit crustal flow (Rippe and Unsworth, 2010). These studies have also focused on some of the major strike-slip faults in Northern Tibet (Bedrosian et al., 2001; Le Pape et al., 2012; Unsworth et al., 2004). Many of these studies were made as part of the INDEPTH project (InterNational DEep Profiling of Tibet and the Himalaya) which has undertaken a series of integrated geological and geophysical studies across the Tibetan Plateau since 1993 (Nelson et al., 1996). INDEPTH-IV was the final stage of this project and focused on the northern margin of the plateau (Karplus et al., 2011; Wei et al., 2014). As part of this study, MT profiles were acquired across the central Altyn Tagh Fault (ATF) in 2010 to investigate the resistivity structure of the lithosphere and thereby constrain deformational processes and test competing models on deformation patterns along the northwestern margin of the plateau (Fig. 1). In this paper, we present new models of the electrical resistivity structure of the central ATF and discuss their interpretation. Insight gained from the Altyn Tagh Fault can give an improved understanding of orogens where continent–continent collisions are active and major strike-slip zones have developed (Eastern Anatolia), as well as those preserved in the geological record.

2. Previous geological and geophysical studies

2.1. Fault geometry

The Altyn Tagh Fault (ATF) is a major boundary that separates the Tibetan Plateau, with an average elevation of more than 4500 m above sea level, from the Tarim Basin, with an elevation of only about 1000 m (Fig. 1). The ATF extends for at least 1500 km from the West Kunlun Mountains in the west to the Qilian mountains in the northeast, and may extend even further northeast for as much as 2500 km (Darby et al., 2005; Mériaux et al., 2005). The ATF can be divided into three main sections based on its geomorphological expression: (a) the southwestern section west of 84°E, (b) the central section between 84°E and 94°E, and (c) the northeastern section east of 94°E. The central section investigated in this study includes several restraining bends where relatively high elevations have been formed by transpressional deformation (Cowgill et al., 2004).

A major splay of the ATF – the North Altyn Fault (NAF, Fig. 1) is located between 86° and 92°E, and is almost parallel to the main ATF (Cowgill et al., 2000). The NAF bounds the Altyn Tagh Range (ATR) together with the ATF to the south and the Lapeiquan Fault to the northeast (Fig. 1). Two different models have been proposed to describe the tectonics of the ATR. One model suggests that the NAF is a thrust fault formed by the southward underthrusting of the Tarim Block, with the ATF acting as a sinistral strike-slip fault (Avouac and Tapponnier, 1993; Burchfiel et al., 1989; Molnar et al., 1987; Peltzer and Saucier, 1996; Wittlinger et al., 1998; Yue et al., 2004). The other model proposes that the ATR is a strike-slip duplex, comprising a group of imbricated blocks bounded by the strike-slip ATF and oblique-slip NAF (Cowgill et al., 2000). Reconstruction of the ATF based on geochronology studies also suggests that the NAF may have been the active trace of the ATF at an early stage of its development (Cowgill et al., 2003).

2.2. Geology

The MT profiles presented in this paper are focused on the central section of the ATF (see Fig. 1). Within this region, the ATF separates the sedimentary fill of the western Qaidam Basin from the Precambrian basement rocks of the Tarim Basin (Wittlinger et al., 1998). Archean and Proterozoic metamorphic rocks are sheared along the fault zone, with coal-bearing Jurassic sedimentary rocks scattered throughout the region (Chen et al., 2003). As shown in Fig. 2, geological units on both sides of the ATF are well correlated. Precambrian complexes are found to the northeast of the Lapeiquan Fault and the North Qilian Fault, while Paleozoic complexes are located to the southwest of the Lapeiquan Fault and the North Qilian Fault (Sobel and Arnaud, 1999). The surface structure of the ATR and the Qilian Block are comprised of primarily Neoproterozoic to Mesozoic sedimentary rocks. Two belts of High Pressure (HP) and Ultrahigh Pressure (UHP) metamorphic complexes, where samples of eclogites and garnet peridotites are found (Gilotti, 2013; Liou et al., 2009; Yang et al., 2001), are located to the south of the ATR (Liu et al., 2012, 2009) and along the northeastern margin of the Qaidam Basin. Accordingly, it was suggested that the geologic units on both sides of the ATF are offset by 475 ± 70 km of sinistral strike-slip motion (Cowgill et al., 2003; Peltzer and Tapponnier, 1988; Ritts and Biffi, 2000).

2.3. Kinematics

As a major strike-slip fault, the ATF plays an important role in accommodating the convergence between the Indian and Eurasian plates. Two different end-member models have been proposed to explain how this convergence occurs. In one class of models it is assumed that the crust is made up of rigid blocks separated by weak fault zones, and convergence is accommodated by deformation along major thrusts and strike-slip faults bounding these blocks (Calais et al., 2006; Meade, 2007; Peltzer and Tapponnier, 1988; Tapponnier and Molnar, 1976; Tapponnier et al., 2001; Thatcher, 2007). This rigid block model regards the eastward extrusion along the ATF as the dominant tectonic mechanism on the northern margin of the Tibetan Plateau. The other class of

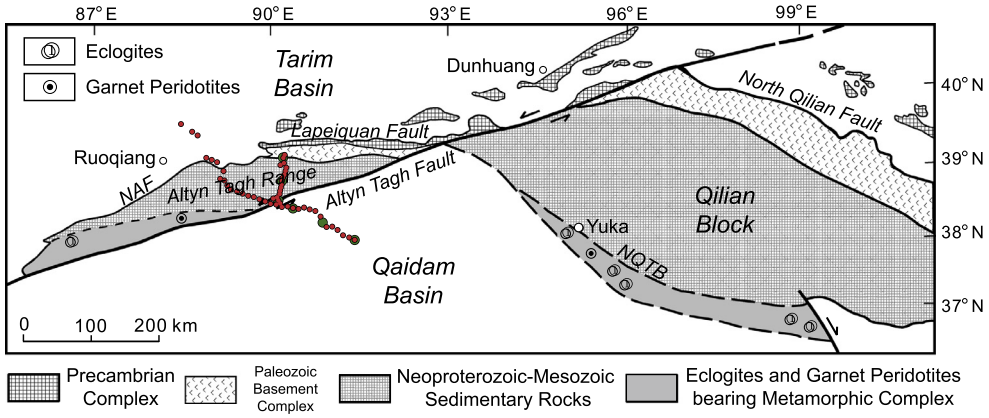

Fig. 2. Simplified geology map of the study area. Base map is after Zhang et al. (2007a). White regions show regions of sedimentary cover in the Tarim and Qaidam Basins. Red dots are broadband MT stations, and green dots are long-period MT stations. Abbreviations are: NAF, North Altyn Fault; NQTB, North Qaidam Thrust Belt. (For interpretation of the references to color in this figure legend, the reader is referred to the web version of this article.)

models assume that the crust deforms viscously with deformation distributed over a broad region, and convergence is mainly accommodated by continuous deformation within the middle to lower crust (Clark and Royden, 2000; England and McKenzie, 1982; England et al., 1988; Royden et al., 1997; Shen et al., 2001a). Thus, according to this continuum model the northern margin of the Tibetan Plateau is characterized by crustal thickening caused by the soft middle to lower crust of the Tibetan Plateau interacting with the rigid Tarim Block. Although it is vigorously debated which model is a more appropriate description of the tectonic processes, it is evident from the presence of major strike-slip faults that horizontal motions are clearly important.

The slip rate along the ATF is an important factor in determining the total contribution from horizontal motion to the overall mass balance of the orogen, and consequently crucial to discriminating between the two different end-member models. A total displacement of $\sim 475 \pm 70$ km has been estimated for the ATF since the mid-Oligocene (Cowgill et al., 2003; Peltzer and Tapponnier, 1988; Ritts and Biffi, 2000). Early slip rate estimates on the ATF vary by a factor of five, depending on which approach was used for the determination. Morphochronological slip rates previously yielded fast prior slip measurements of 20 mm/yr or more (Mériaux et al., 2004, 2005; Peltzer et al., 1989), whereas geodetic techniques gave relatively slow present-day slip rates of $\sim$10 mm/yr (Bendick et al., 2000; Chen et al., 2000; Elliott et al., 2008; Shen et al., 2001b; Wallace et al., 2004; Zhang et al., 2007b). This difference was first reconciled by Cowgill et al. (2009), and recent geodetic (He et al., 2013), paleoseismic (Washburn et al., 2003, 2001), and geologic data (Cowgill et al., 2009; Gold et al., 2011) all agree on a Late Quaternary rate of 9.0 ± 4.0 mm/yr. Although the majority of these studies focused on the central ATF, an important issue in slip rate comparisons is the observed eastward decrease in slip rate. Meyer et al. (1996) concluded that the slip rates east of 96°E are just 4 ± 2 mm/yr, and this slip gradient has been accommodated by thrusting along the margins of the Qaidam Basin (Mériaux et al., 2012).

2.4. Previous geophysical studies

A gravity survey of the central ATF suggested that the fault is sub-vertical and penetrates the entire lithosphere (Jiang et al., 2004). Seismic studies of the central ATF include the teleseismic tomography experiment by Wittlinger et al. (1998) that showed a low P-wave velocity anomaly extending to a depth of 140 km. This anomaly suggested that the ATF is lithospheric in scale and was interpreted as faulted rocks, including asbestos-rich serpentinite bodies, in the shallower part and a ductile shear zone at greater depth. The interpretation of their model also proposed that convergence had occurred across the ATF, with the lithosphere of the Tarim Basin being thrust beneath the Tibetan Plateau, making the ATF behave as an oblique plate boundary. Herquel et al. (1999) observed teleseismic shear wave splitting in the same region, and found that the delay times displayed a marked increase in a narrow zone centered on the ATF, implying anisotropy within the lithospheric mantle. Their results add additional support to the thesis that the ATF guides the northeastward extrusion of the Tibetan lithosphere.

Zhao et al. (2006) studied the crustal and uppermost mantle structure across the ATR and its adjacent basins by using the refraction/wide-angle-reflection data from an active-source seismic profile. They reported a wedge-shaped low-velocity zone extending to the depth of about 90 km beneath the ATR, which was interpreted as a mixture of mafic crustal and ultramafic mantle material. They proposed a model for the ATR that included southwestward underthrusting of a sliver of the easternmost Tarim lithosphere at an oblique angle into the ATR and NE–SW convergence within the range. Seismic studies have revealed that the crustal thickness of the adjacent Tarim Block and the Tibetan Plateau are 40–50 km and 60–70 km respectively, although it is still controversial whether the ATF is of crustal scale (Zhao et al., 2006) or lithospheric scale (Wittlinger et al., 1998).

According to the distribution of earthquake focal mechanism solutions in the study area (see Fig. 1), earthquakes occurring close to the ATF mostly exhibit strike-slip mechanisms, whereas earthquakes located to the south of ATF were mostly produced by compressional processes along the thrust faults on the western margin of Qaidam Basin.

Paleomagnetic studies infer that no vertical-axis rotation of the Qaidam Basin or the ATF has occurred in the Neogene, which means the displacement between the Tarim Basin and the Tibetan Plateau is mainly accommodated by the strike-slip motion along the ATF rather than distributed shearing deformation within the northern Tibetan Plateau (Dupont-Nivet et al., 2002).

Previous MT studies were mainly focused on the northeastern ATF, in which the ATF was imaged as a sub-vertical electrical resistivity boundary that shallowed to the east (Bedrosian et al., 2001; Xiao et al., 2011). However, the electrical resistivity structures beneath the central ATF, where the seismic studies were mainly located, were unknown prior to the INDEPTH-IV investigations. In this study, MT data are used to provide new constraints to distinguish between competing tectonic models for the northern margin of the Tibetan Plateau. MT data are inherently sensitive to the presence of fluids, both aqueous and partial melt, which weaken crustal material. Thus resistivity models derived from MT

can define the geometry of fluid zones that often control the deformation style.

3. MT data acquisition

MT data were recorded along the profiles shown in Fig. 1 and included both broadband MT (BBMT) and long period MT (LMT) data. The BBMT data were collected with Phoenix MTU-5 instruments, and LMT data with LEMI-417 instruments. All five components of the time-varying electromagnetic field (E_x, E_y, H_x, H_y, H_z) were recorded. As shown in Fig. 1, the profile crosses the central ATF close to the town of Mangai. To the north of the ATF, the profile splits into two branches (Line1 and Line2, see Fig. 1). The total survey consisted of 50 BBMT stations (red dots in Fig. 1) and 6 LMT stations (green dots in Fig. 1). The average station spacing was 5 km and 40 km for the BBMT and LMT instruments respectively. The original MT time series data were transformed into the frequency domain, and frequency dependent transfer function elements were computed through remote-reference processing with statistically robust algorithms (Egbert, 1997; Jones and Jödicke, 1984; Varentsov et al., 2003; Wight et al., 1977). With an average recording time of 20 hours for BBMT, high quality MT data were obtained in the period range of 0.003–2000 s. The LMT stations provided useful data in the period range 100 to 10,000 s from an average recording duration of 20 days. Note that the BBMT and LMT stations were deployed in different years and were not in exactly the same locations. Thus, the LMT responses were used as independent stations and were not merged with the broadband stations during inversion. Typical sounding curves (Fig. S1) and related discussions are presented in supplementary file 1.

4. MT data analyses

The goal of MT data analysis is to derive a dataset suitable for defining the resistivity model of the Earth from the observed MT data. It is therefore essential to investigate the dimensionality of the MT responses, and determine if the data require a 1-D layered Earth, 2-D model invariant in the strike direction or 3-D resistivity model. The phase tensor (Booker, 2014; Caldwell et al., 2004) is a useful tool in assessing the dimensionality of MT impedance data and is defined as the product of inverse real matrix and imaginary matrix of the impedance tensor. It can be graphically represented as an ellipse defined by three values: the maximum phase Φ_{max}, the minimum phase Φ_{min}, and the skew angle β. Φ_{max} and Φ_{min} correspond to the major and minor axes of the ellipse with their directions indicating the two orthogonal electrical principal axes, or two possible strike directions. Under 1-D conditions, Φ_{max} and Φ_{min} are equal and the ellipse is a circle. The skew angle (β) gives a measure of the dimensionality and is defined by Caldwell et al. (2004). The skew is zero for a 1-D or 2-D resistivity structures, and non-zero values indicate a 3-D resistivity structure.

The phase tensor maps are plotted in Fig. 3, and most of the stations showed relatively small skew angles at short periods ($<5°$, as shown in blue, see Fig. 3a–b). In Fig. 3a, many stations exhibit one-dimensionality as indicated by the phase tensor plotting as a circle, which is reflecting the shallow sedimentary units in the Tarim and Qaidam Basins. However, at longer periods some stations start to exhibit complex aspects, which do not support the presence of a 2-D resistivity structure ($\beta > 10°$, as shown in yellow and red colors, see Fig. 3c–d). However, such stations are relatively sparsely distributed, which indicate that the 3-D effects are generally localized. Statistical analysis of the directions of Φ_{max} and Φ_{min} are also shown as rose diagrams in Fig. 3. It can be seen that the distribution of these directions are quite scattered at short periods and no dominant direction can be determined (see Fig. 3a–b). This is probably due to the one-dimensionality of the shallow sedimentary layer in the Tarim and Qaidam Basins. At longer periods (Fig. 3c–d), a relatively consistent strike direction (~N70°E) can be observed, which is closely parallel to the surface trace of the ATF.

Further analyses were also conducted utilizing multi-site, multi-frequency tensor decomposition technique of McNeice and Jones (2001) and induction vectors (Parkinson, 1959). Details of these analyses results are presented in the supplementary material and the conclusions are generally consistent with phase tensor analyses, which suggest that the data are generally of two-dimensional, but with some localized 3-D effects, and a regional strike direction of N70°E. The NW-SE trending thrusts to the south of the ATF on the western margin of the Qaidam Basin are probably the sources of the observed 3-D effects. Consequently, in this study, both 2-D and 3-D inversions were used, and a joint interpretation was made on the basis of these two types of resistivity models.

5. MT data inversion

5.1. Two-dimensional (2-D) inversion

The MT stations were divided into two profiles labeled Line1 (4200–4330–4510) and Line2 (4200–4330–4410n), and were inverted separately. These two profiles share the same MT stations south of the ATF but differ in their northwestern sections. The MT data were decomposed into two independent modes, namely, the transverse electric mode (TE) and the transverse magnetic mode (TM) along the regional strike direction N70°E, and inverted with the 2-D nonlinear conjugate gradients (NLCG) algorithm of Rodi and Mackie (2001). Both TE and TM modes, and the vertical magnetic field transfer function (tipper) data in the 6-decade period range of 0.01–10,000 s were used in 2-D inversion. The same inversion parameters were applied to both profiles (Line1 and Line2) to ensure that the inversion models were comparable. The error floors for the TM apparent resistivity and phase data were set to 10% and 1.45° (equivalent to 5% in apparent resistivity) respectively. Given that the TE mode data can be more susceptible to 3-D effects than the TM mode data (Becken et al., 2008; Jones, 1983; Wannamaker et al., 1984), relatively high error floors of 40% and 2.9° (10% in apparent resistivity) were applied to the TE apparent resistivity and phase data, respectively, to reduce the weight of the TE data in the 2-D inversions. For the tipper data, an absolute error floor of 0.05 was applied. A horizontal smoothing factor of $\alpha = 1$ was used, which imposes equal smoothness in the horizontal and vertical directions. The roughness regularization parameter $\tau = 3$ was determined through a trade-off analyses, which corresponds to the corner of the L-curve (see Fig. S8) between overall root-mean-square (r.m.s.) misfits and model norms (Hansen, 1992; Hansen and O'Leary, 1993). All inversions were started from a 100 Ω m uniform half space. Preferred models that fit the MT data with overall r.m.s. misfits of 1.897 (Line1) and 1.872 (Line2) are presented in Fig. 4 along with their site-by-site misfit distributions.

From the 2-D inversion models, four major conductors and two resistors were identified and are marked as C1–C4 and R1–R2 in Fig. 4. Features C1 and C2 are located beneath the Qaidam Block south of the ATF. C1 is located at lower crustal to upper mantle depths, whereas C2 is located in the middle to lower crust. Conductor C3 is located in the upper crust directly beneath the ATF, and the large-scale south-dipping conductor C4 extends from surface to upper mantle beneath the ATR to the south of NAF. Resistor R1 is located in the upper to middle crust beneath the Qaidam Block, whereas R2, which is much more resistive, is located beneath the Tarim Block to the north of the NAF. Features C1–C3 and R1 were detected on both profiles, whereas C4 and R2 were only imaged on Line1.

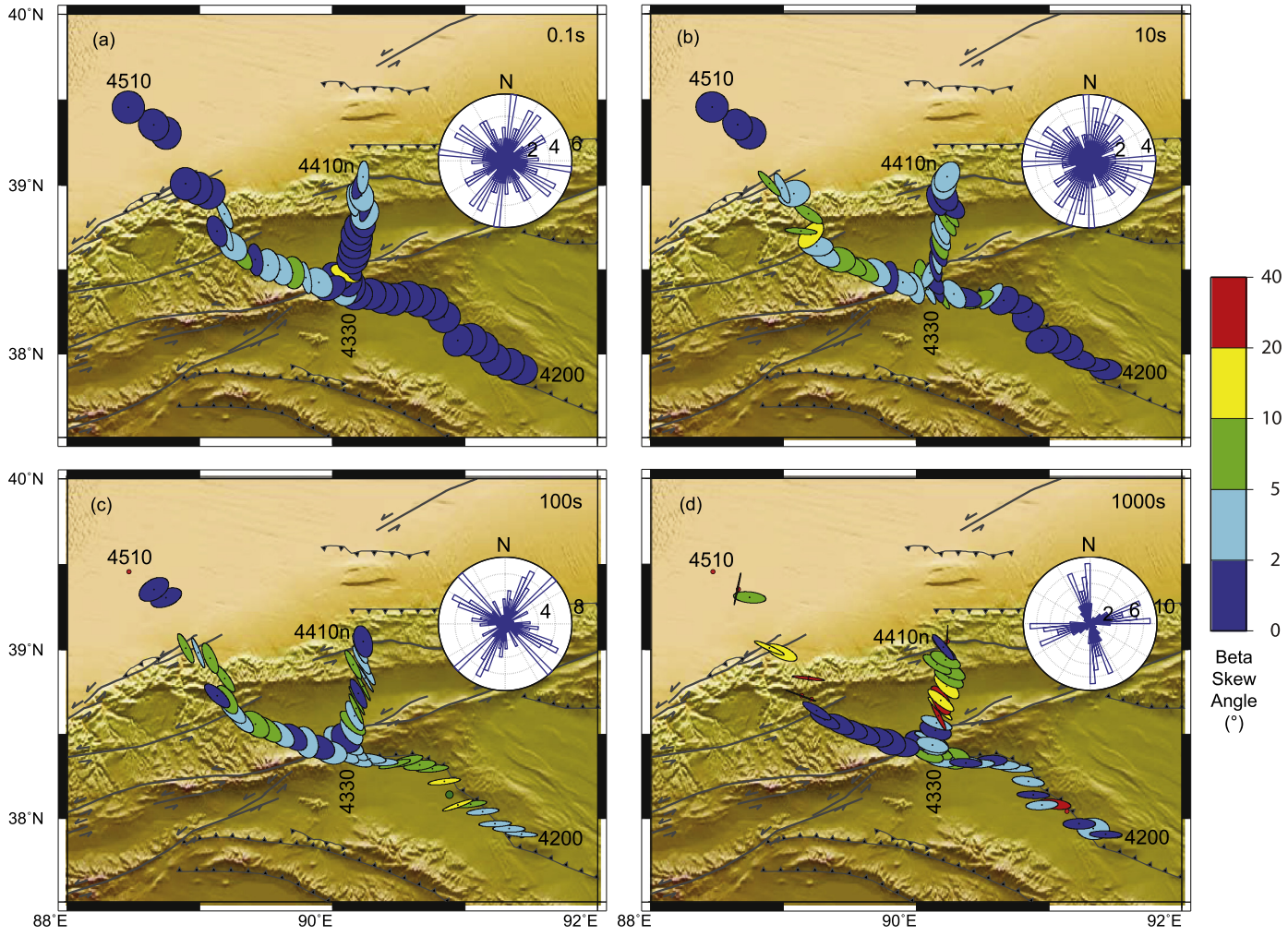

Fig. 3. Phase tensor maps for periods of (a) 0.1 s, (b) 10 s, (c) 100 s, and (d) 1000 s. Rose diagrams show the statistical results of directions of Φ_{max} and Φ_{min} for each period.

Line1 and Line2 share the same stations in their southern sections, and from these two models, the geometries of anomalies C1, C3 and R1 are generally consistent, which is as expected as they were imaged using the same data. However, there is a large difference in the spatial scale of conductor C2. The scale of C2 is far larger on Line2 than on Line1, and its lower boundary is also much deeper on Line2 than Line1. This difference may be caused by some off-profile 3-D distortions originated from the thrust belts to the south of ATF on the western margin of the Qaidam Block, as discussed in data analyses section. Such 3-D features cannot be robustly resolved through a 2-D approach. Consequently, 3-D inversions were conducted to further investigate these features.

5.2. Three-dimensional (3-D) inversion

Inversion of MT data on a 2-D profile with a 3-D algorithm not only images the subsurface electrical resistivity structure beneath the profile, but also can qualitatively constrain the geometry of off-profile structures that cannot be correctly resolved with a 2-D approach (Siripunvaraporn et al., 2005b). In this study, the WSINV3DMT code developed by Siripunvaraporn et al. (2009, 2005a) was used for 3-D inversion.

The starting model was a uniform 100 Ω m half space with 53, 70 and 47 cells in the north–south, east–west and vertical directions respectively, including 7 air layers. Forty-six MT stations with relatively high data quality were selected for the 3-D inversion, and 24 frequencies were extracted for each station within the 6-decade wide period range of 0.01–10,000 s, with 4 frequencies per decade. The full impedance tensor and tipper were inverted to ensure that off-profile structures were resolved as reliably as possible (Siripunvaraporn et al., 2005b). A uniform error floor of $0.05 \cdot (Z_{xy} \cdot Z_{yx})^{1/2}$ was applied to all four impedance tensor elements. An error floor of $0.1 \cdot [(T_{zx})^2 + (T_{zy})^2]^{1/2}$ was applied to all two vertical magnetic field transfer function elements. Length scale parameters of $\tau = 5$, $\delta x = \delta y = \delta z = 0.1$, and Lagrange multiplier parameters of initial value $\lambda = 3$, step $= 0.5$ were used during the 3-D inversion.

Initially the inversion was run for 10 iterations. Then the model from the iteration with the lowest misfit was selected as the initial and a priori model for the next round of 10 iterations with all other parameters unchanged. After three rounds of 3-D inversions, the inversion was observed to have converged, based on the fact that the resistivity model was not varying significantly from iteration to iteration. The preferred model has an r.m.s. misfit of 3.127 and was selected as is the inversion model from the 4th iteration in the 3rd round of inversions. This type of multi-stage inversion scheme was proven to be able to decrease both data misfit and model norm effectively (Xiao et al., 2012). Horizontal slices of the 3-D model at depths of 30, 50, 70, and 90 km are plotted in Figs. 5a–d. Misfit variation during the inversion process and site-by-site r.m.s. distribution are shown in Figs. 5e and 5f. It can be seen that there is only one station with r.m.s. misfit over 4, and misfits of most stations are less than 4, which indicates a rea-

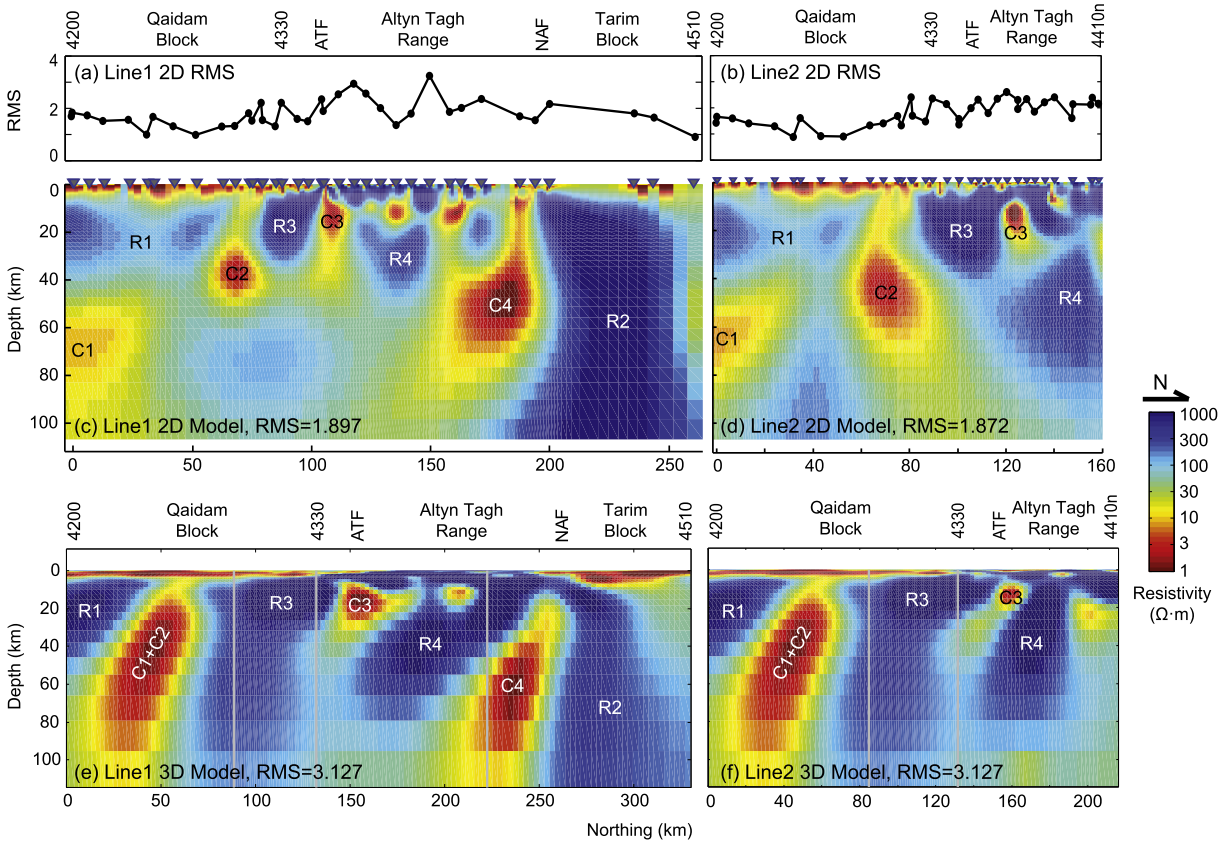

Fig. 4. 2-D and 3-D inversion models for (c, e) Line1 and (d, f) Line2, as well as (a, b) site-by-site r.m.s. distributions for 2-D inversion models. Locations of vertical slices from 3-D inversion model are shown in Fig. 5c with gray lines indicating turning points. Abbreviations are: ATF, Altyn Tagh Fault; NAF, North Altyn Fault; C1–C4 are conductors and R1–R4 are resistors.

sonable data fit. The fit of the 3-D model to the measured data is illustrated in the supplementary material.

5.3. Comparison of 2-D and 3-D inversion models and resolution tests

Vertical cross sections were extracted from the final 3-D inversion model to compare with the 2-D inversion models (see Fig. 4). Electrical resistivity features C3, C4, R1 and R2 are imaged by both inversions models, and generally have consistent geometries. However, C1 and C2 from the 2-D inversion are actually imaged as a single conductor rising from the upper mantle to the upper crust in the 3-D inversion model (see C1 + C2 in Figs. 4e and 4f). We consider this combined C1 + C2 feature from the 3-D inversion model to be more reliable, given the relatively complex dimensionality to the south of the ATF as discussed above.

By conducting 3-D inversions on 2-D MT profile data, off-profile structures, especially conductors, can be qualitatively imaged (Siripunvaraporn et al., 2005b). From Figs. 5a–d, it can be seen that conductors C1 + C2 and C4 are related to off-profile features which both extend eastward. Although the geometries of these off-profile conductors cannot be well-constrained due to the lack of data, these conductors are required to fit the observed MT data. Consequently, their horizontal spatial extension can be reasonably and qualitatively constrained as extending eastward.

MT data are generally most sensitive to the depth to the top of a conductor, while the base of conductors are not well resolved. Thus the horizontal position and dip of a low resistivity feature can be well constrained. A consequence of the smoothing imposed in inversions is that conductors will be smeared downwards. In terms of a dipping structure such as C4, the depth and southward dip of this feature are well resolved. To further constrain the depth extent of conductors C1 + C2 and C4, a 3-D forward modeling study was implemented by calculating the responses from a modified 3-D resistivity model and observing the change in r.m.s. misfits to ascertain if the data are sensitive to these modifications. The 3-D forward model was obtained by removing conductors C1 + C2 and C4 from the model in Fig. 5 below 90 km depth and the region was set to a 100 Ω m uniform half space. The new response data were computed with forward modeling and the resulting site-by-site r.m.s. misfit variation is plotted in Fig. 6. The response curves are shown in the supplementary material. It can be observed that there is a systematic increase in r.m.s. misfits at most stations in the modified model. Although a few stations show a decrease in r.m.s. misfits, their reduced percentages are much smaller than those stations showing increases. Furthermore, stations above or close to the regions of C1 + C2 and C4 generally showed greater increases in r.m.s. misfit. All these features suggest that the MT data are sensitive depths of at least 90 km, and the vertical extension of conductors C1 + C2 and C4 are no less than 90 km.

6. Model interpretation and discussion

In interpreting the resistivity model, previously published seismic models (Wittlinger et al., 1998; Zhao et al., 2006), and potential field and surface heat flow data (Zhao et al., 2010) were used in the interpretation. In this section, each part of the model is discussed and the resistivity models are compared with the seismic velocity models as well as other datasets (Fig. 7). Note that Line1 and Line2 diverge north of 4330 which is to the south of the ATF, and the resistivity models are different on each line.

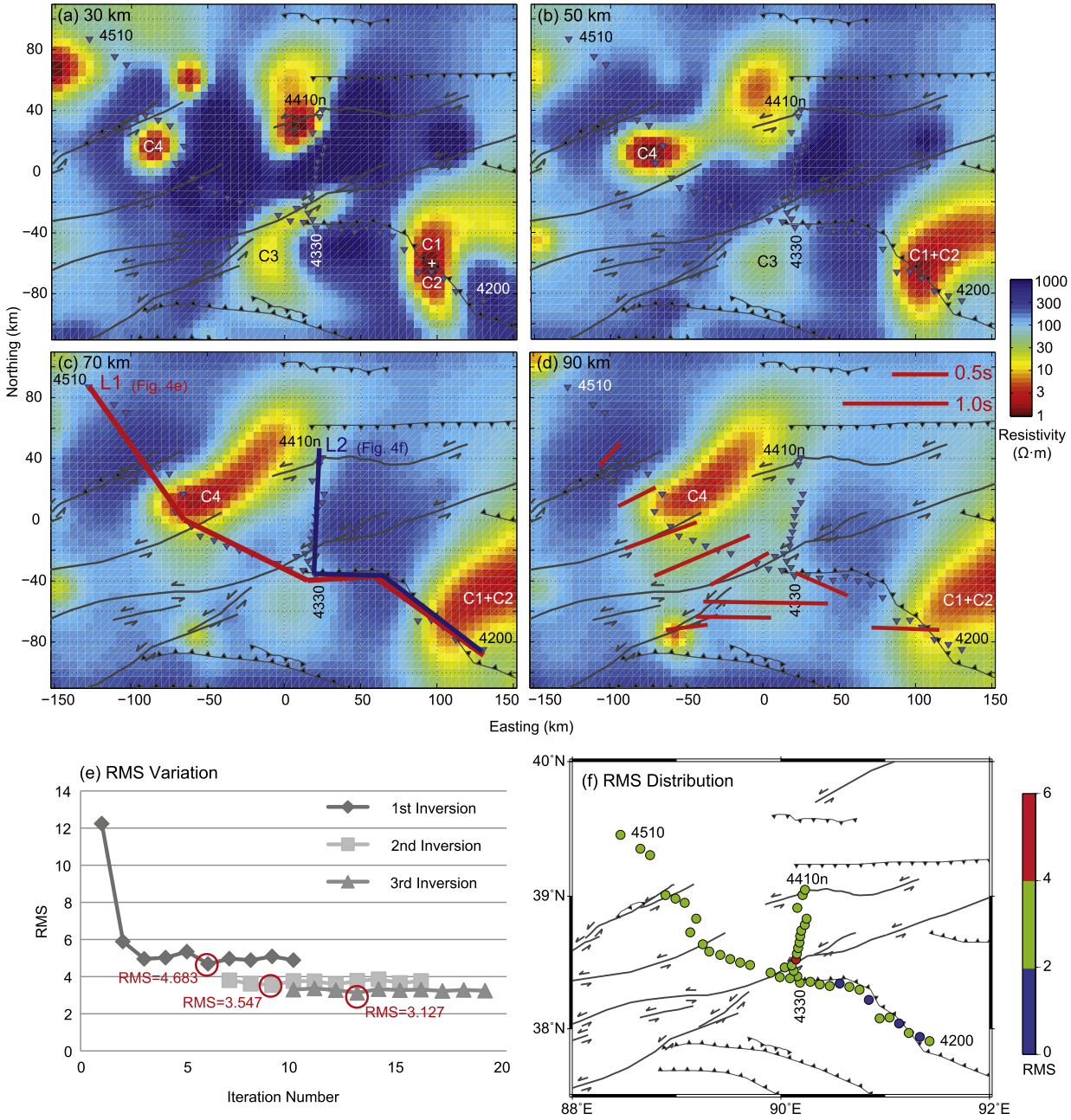

Fig. 5. (a)–(d) Horizontal slices extracted from 3-D inversion model. (e) R.m.s. misfit variation during the process of 3-D inversion. (f) Site-by-site r.m.s. misfit distribution. Red line L1 and blue line L2 in (c) show the location of vertical sections from 3-D inversion model in Fig. 4. Red bars in (d) show the observed teleseismic shear wave splitting from the study of Herquel et al. (1999).

6.1. The Altyn Tagh Fault

In both of the 2-D and 3-D inversion models presented in this paper, the electrical structure beneath the ATF is characterized by a sub-vertical conductor C3, which is separated from a larger conductor C4 by resistor R4. Other upper crustal conductors similar to C3 are present.

Conductor C3 is directly below the fault trace, a location where MT studies of other fault zones have reported major conductors that have been interpreted as elevated concentrations of aqueous fluids. C3 is similar in geometry and conductivity to the conductors detected beneath the San Andreas Fault (Becken et al., 2011) and East Anatolian Fault (Türkoğlu et al., 2015). Wittlinger et al. (1998) used seismic tomography to image the ATF and reported a sub-vertical low velocity zone (LVZ) that extended from the surface to a depth of 140 km (Fig. 7a). They proposed that the ATF was lithospheric scale shear zone with the low velocity anomaly interpreted as a zone of faulted rocks with enhanced porosity and fluid content. The geometry of the anomaly in the MT model is similar to the seismic anomaly. It should be noted that the tomographic technique used by Wittlinger et al. (1998) used sub-parallel rays that may give limited depth resolution (Lévêque and Masson, 1999). The coincident anomalies in resistivity and velocity may reflect a common origin, i.e. both rock properties will be reduced by the presence of elevated porosity. The comparison between the resistivity anomaly and seismic velocity anomaly may also be influenced by other minerals present in the fault zone. Serpentinite has been mapped along the central ATF and at Mangai, where the MT western profile crosses the trace of the ATF (see Fig. 1), serpentinite bodies rich in asbestos and talc have been mined

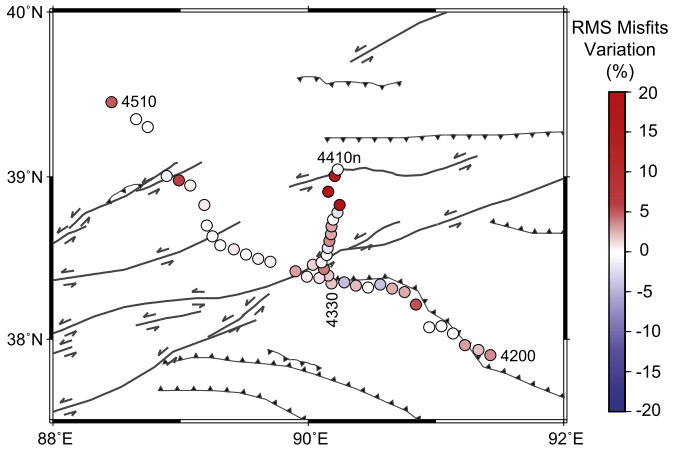

Fig. 6. Distribution of r.m.s. misfits variation of a 3-D forward model with structures beneath 90 km modified to 100 Ω m from the original 3-D inversion model.

(Xinjiang Bureau of Geology and Mineral Resources, 1993). The soft slippery mineral talc could facilitate creep on the central ATF, as previously discovered in the creeping section of the San Andreas Fault (Moore and Rymer, 2007). Serpentinization reduces seismic velocity (Hyndman and Peacock, 2003), and could provide contribute to the sub-vertical LVZ reported by Wittlinger et al. (1998). In contrast, serpentinite has a high electrical resistivity (>10,000 m) similar to other dry mantle minerals (Guo et al., 2011; Reynard et al., 2011). Thus the presence of serpentinite would increase the scale of seismic anomaly, while not affecting the resistivity anomaly. Serpentinization can cause the precipitation of magnetite (Evans et al., 2013), and if present in high concentrations the magnetite may increase conductivity (Kawano et al., 2012) and produce detectable magnetic anomalies at the surface. Fig. 7c shows some correlation between conductance (integrated conductivity) and magnetic anomaly within the ATR. The conductance integrated from the surface to a depth of 50 km and 100 km is shown in Figs. 7e and 7g. The 50 km depth corresponds to the Curie isotherm (∼580 °C) as estimated by Zhao et al. (2010). Relatively large magnetic anomalies are observed directly above the ATF and the NAF, which are also two regions with high conductance (Fig. 7e). The seismic study of Zhao et al. (2006) did not report a major LVZ beneath the ATF, but this may be because the survey geometry was optimized for detection of sub-horizontal structures.

Conductor C4 is stronger than C3 and a model of the ATF must account for its origin. One possibility is that the low resistivity is due to graphite films, which have been proposed as the cause of low resistivities in a number of ancient suture zones, e.g. Rao et al. (2014). A possible suture in this part of the Altyn Tagh area was proposed by Sobel and Arnaud (1999) and named the Lapeiquan suture. The geometry was proposed to be south dipping, which matches the geometry of C4. A problem with invoking graphite as an explanation for the low resistivity, is that graphite films do not remain connected above temperatures of 700 °C (Yoshino and Noritake, 2011). Based on the geothermal gradient of 28–34 °C/km reported by (Zhao et al., 2010) this would occur at a depth of 23–25 km, well above the depth of anomaly C4.

Aqueous fluids provide an alternate explanation for C4, but a mechanism to create them must be determined. One mechanism that could generate fluids is the underthrusting of crustal rocks which then undergo prograde metamorphic reactions with the increasing temperature and pressure. These fluids will be saline and produce a zone of low resistivity such as C4. This type of process has been inferred from MT studies of a number of convergent plate boundaries where crustal thickening has occurred (Bertrand et al., 2009; Wannamaker et al., 2002). Fluids will flow to the surface through the highest permeability pathways, i.e. faults. In this case, fluids are generated due to the oblique underthrusting of the Tarim Block beneath the northern Tibet along the NAF, and the ATF system provides a pathway for the fluids to move upwards. As the fluids migrate to the surface, they can cause metasomatic reactions such as serpentinization (Hyndman and Peacock, 2003). However, it should be noted that no surface outcrop of serpentinite has been reported (Eric Cowgill, personal communication, 2014).

Is this mechanism of fluid generation consistent with other geological and geophysical data? It is significant that C4 does not produce a major low seismic velocity anomaly in either the Wittlinger et al. (1998) or Zhao et al. (2006) models. This can be explained if the fluid has a high salinity, with only a small concentration needed to produce the observed high conductivity. The seismic model of Wittlinger et al. (1998) gives evidence that underthrusting has occurred. While Zhao et al. (2006) reported a relatively flat Moho beneath the ATF (Fig. 7b), they also describe an anomalously slow region in the upper mantle that was partially due to the presence of crustal material. While both these models propose some degree of fault normal shortening, the maximum amount is constrained by structural studies based on seismic reflection data from the Tarim Basin (McDermott et al., 2014) to a few kilometers. It should be noted that these observations do not constrain the amount of motion of the entire Tarim block – just the internal deformation. The geothermal gradient beneath Qaidam was reported as 28-34 °C/km Qaidam (Zhao et al., 2010). Thus with an average value of 30 °C/km, a change in depth from 7–9 km would correspond to a temperature change of 210–270 °C, sufficient for the transformation from greenschist to amphibolite or amphibolite to granulite facies. These prograde metamorphic reactions both generate water through the corresponding mineral reactions.

In summary, we propose that the ATF system is characterized by fluid generation in a deep fluid-rich zone, with faults acting as a migration pathways for the upwelling fluids. Both seismic models report some local thickening of the crust beneath the ATR, which could produce fluids. If the Moho was indeed flat, then this could be incompatible with our model, as a source of fluid in the mantle is more difficult to justify. Thus the presence of an anomalous region at, and just below, the Moho in the model of Zhao et al. (2006) helps reconcile the seismic and resistivity models. Note that the mixing of mafic and ultramafic rocks will not produce a major change in resistivity. It is the fluid generation that gives an observable resistivity anomaly.

Could the fluids originate elsewhere? One possible interpretation is that the fluids responsible for C4 are generated within the thickened Tibetan crust adjacent to the ATF at depth. In this case, underthrusting would not be required, although horizontal transport of fluids could be difficult to explain, and the resistive zone at depth beneath the ATF is likely a barrier. Lateral flow of lower Tibetan crust has been widely invoked to explain a number of observations of crustal structure in Tibet – but is unlikely to be in operation here because transpressional deformation may be only restricted to the strike-slip duplex of the ATR (Cowgill et al., 2000). Another possibility is that the fluids are generated by shear heating and related magmatic processes in the deep crust, as envisioned by Leloup et al. (1999) based on exhumed shear zones and numerical simulations.

6.2. Crustal structure of the Qaidam Block

The electrical structure beneath the Qaidam Basin is different in the 2-D and 3-D inversion models. Considering that the dimensionality is relatively complex to the south of the ATF, and structures beneath the Qaidam Basin may not be robustly resolved in the 2-D inversion, the 3-D inversion model is used for interpretation.

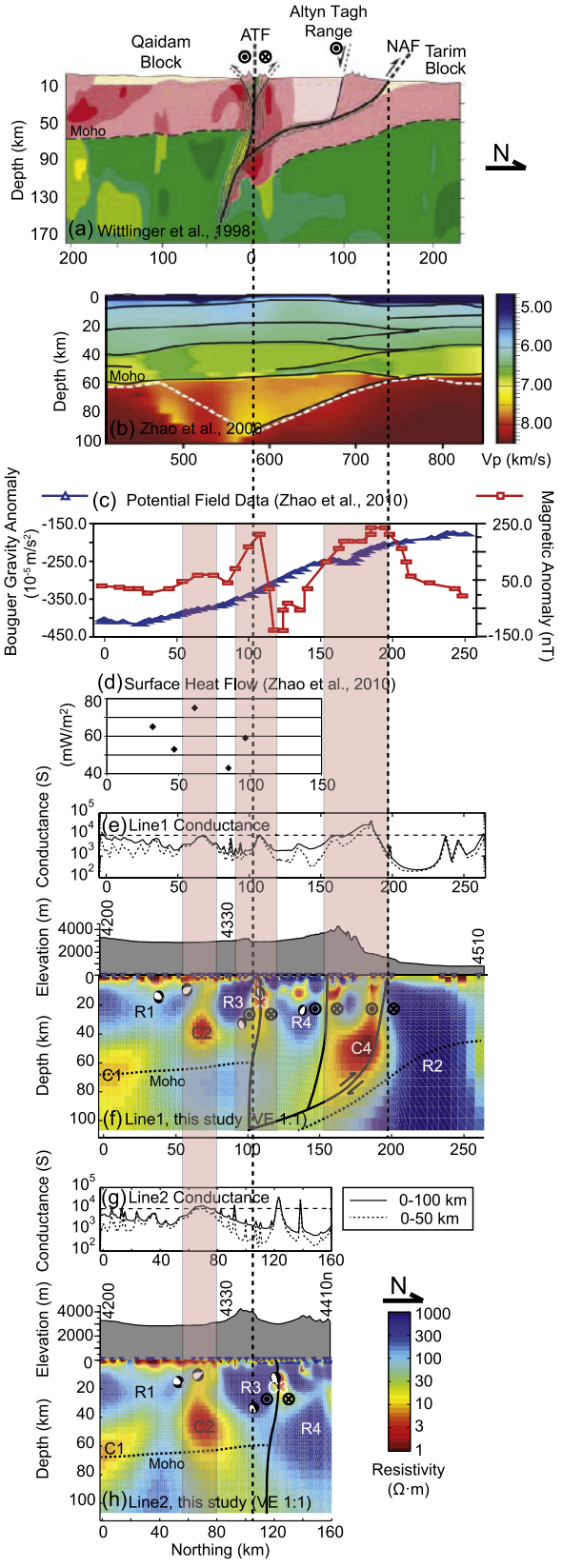

Fig. 7. Comparison between different geophysical models/datasets across the central ATF. (a) Schematic seismic model of Wittlinger et al. (1998). Red and green regions indicate the crust and mantle, respectively. Regions that are more yellow or red in the model are low velocity zones. (b) Seismic model of Zhao et al. (2006). Black lines are inferred discontinuities from the original paper. Regions above the white dashed line are of relatively high resolution due to dense ray coverage. Horizontal distances in (a)–(b) are using coordinates from the original papers. (c) Potential field data from Zhao et al. (2010). (d) Surface heat flow data from Zhao et al. (2010). (e)–(h) Electrical resistivity models for Line1 and Line2 of this study, as well as conductance integrated from surface to the depth of 100 km and 50 km for each profile. Focal mechanism solutions are from the Global CMT Project (http://www.globalcmt.org). Moho depth is after Wittlinger et al. (1998). All subfigures are aligned according to the locations of ATF and NAF (vertical black dashed lines). Pink bars show the highlighted anomalies discussed in this paper.

The 3-D inversion model (Fig. 4e–f), shows that the shallow resistivity structure of the Qaidam Block consists of a thin (<5 km) conductive layer that can be identified as the shallow sedimentary cover of the Qaidam Basin. This is underlain by a heterogeneous layer characterized by several conductors (C1, C2) and resistors (R1, R3). The resistors are associated with the crystalline basement rocks and typical of such rocks. The conductors require an explanation in terms of the material causing the low resistivity.

There are two distinct scenarios for the origin of these fluids. The first is the same as elsewhere in Tibet where crustal thickening has produced elevated temperatures that in the presence of water can lead to melting. In many previous studies of Tibet, conductive layers such as these have been detected and interpreted as fluid rich layers, either partial melt or aqueous fluids (Li et al., 2003; Unsworth et al., 2005; Wei et al., 2001). Thus conductive zones are most likely combinations of aqueous fluids and partial melt. Evidence for elevated temperatures comes from heat flow measurements close to the profile and shown in Fig. 7d. Relatively high heat flow can be observed above conductor C2 in the 2-D inversion model (or the upper part of C1 + C2 in the 3-D inversion model). This could be explained by the elevated temperature in the upper to middle crust caused by upwelling of hot material from the lower crust beneath the Qaidam Basin along the ductile flow path represented by C1 + C2. Using laboratory studies, these layers can be inferred as possible low strength regions that could flow, although MT cannot directly the detect motion (Rippe and Unsworth, 2010). The feature C1 + C2 detected beneath the Qaidam Block is likely similar in composition to those reported elsewhere beneath the Tibetan Plateau. In the model, conductor C1 + C2 may represent a fluid rich region. If this causes sufficient weakening then it could be associated with regional ductile flow path on the western margin of the Qaidam Basin. This proposed flow is also consistent with the observed teleseismic shear wave splitting that shows a roughly E–W extending fast axes direction to the south of the ATF (see Fig. 5d). This observed anisotropy could be explained by the proposed upper mantle flow beneath the Qaidam Basin.

The second possible origin for the fluids causing C1 + C2 is that have been formed by prograde metamorphism in the thickened crust, similar to the explanation proposed for C4 in the previous section. This is supported by the striking similarity of the shapes of conductors C1 + C2 and C4.

The discovery of conductive features at the western margin (this study) and northeastern margin (Xiao et al., 2011) of the Qaidam Basin further raises the possibility that there might be a widespread conductive layer in the lower crust and upper mantle beneath the Qaidam Basin, which could decouple the Qaidam crust and mantle. Such a detachment layer is required by geodynamic models to explain the deformation of the Qaidam Block and surrounding regions, and have been proposed a range of depths from upper crust to upper mantle (Burchfiel et al., 1989; Yin et al., 2008; Yin et al., 2002; Zuza and Yin, 2013). It could further explain how the strike slip motion along the ATF was accommodated by internal deformation within the Qaidam Basin. However, due to the lack of MT data within the basin, it is still unknown whether this layer exists extensively in the interior regions of the Qaidam Basin.

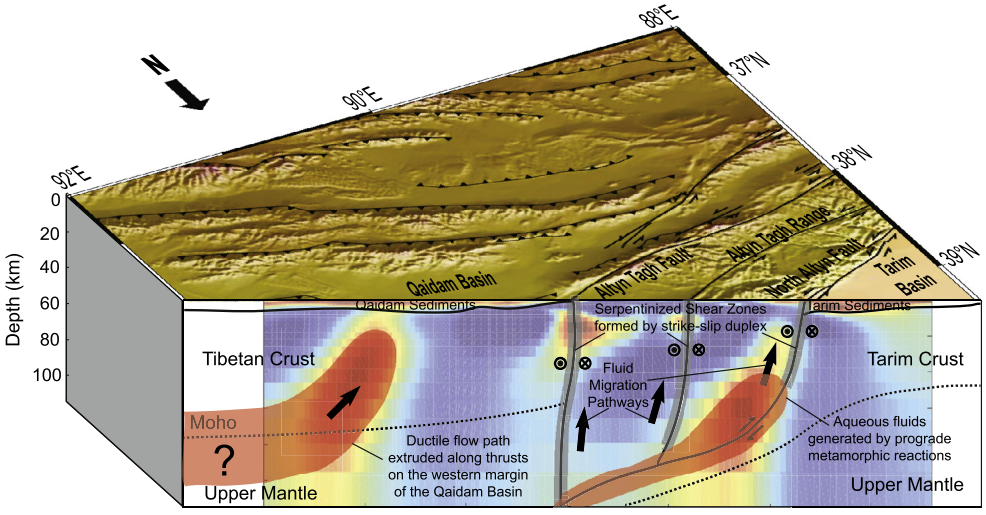

Fig. 8. Model of lithospheric structure across the central ATF on the northern margin of the Tibetan Plateau derived from magnetotelluric and other data.

6.3. Tarim Block

To the north of C4, the Tarim Block is characterized by high resistivity (R2 in Fig. 4) that extends from the surface to the upper mantle. The Tarim Block consists primarily of Neoarchean and Paleoproterozoic rocks overlain by Meso-Neoproterozoic sedimentary cover (Zheng et al., 2013). Sedimentary rocks of the Tarim Block are generally thin in the surrounding margins and thick in the central region, where the thickness locally exceeds 15 km. In both the 2-D and 3-D inversion models, R2 corresponds to the resistive Precambrian basement of the stable Tarim Block, with the shallow conductive layer above R2 representing the sedimentary fill of the Tarim Basin. The contrast between C4 and R2 outlines the oblique-slip NAF as part of a strike-slip duplex that represents the ATR.

6.4. Geodynamic model

Based on the interpretations made above, a model is proposed to describe the convergent process on the northern margin of the Tibetan Plateau. As shown in Fig. 8, this model incorporates (a) a relatively hot and weak northern Tibetan crust that may flow, (b) possible ductile flow motion towards the surface in the western margin of the Qaidam Basin, and (c) thickened crust beneath the ATR produced by limited oblique underthrusting of the Tarim Block along the NAF. Aqueous fluids are generated by prograde metamorphic reactions caused by the underthrusting of Tarim crust, and upwelling along the serpentinized shear zones of ATF system, which act as fluid migration pathways. This model explains diverse geophysical anomalies observed in the study area and brings a new perspective to understanding the continent–continent collision on the northern margin of the Tibetan Plateau. Based on our interpretations, we propose that the rigid block model and continuum model are both applicable for this study region. However, the continuum model seems to be more dominant as evidenced by large scale conductors associated with distributed crustal thickening. It must also be emphasized that the MT data presented in this paper cannot image along strike variations, and further research is needed to determine if the structure at 90°E is representative of other segments of the fault.

7. Conclusions

A magnetotelluric study across the Altyn Tagh fault yielded data that gives new images of the northern boundary of the Tibetan Plateau. The following four points are the most significant:

(1) Dimensionality analyses showed that the MT data are generally two-dimensional but with some localized 3-D effects. Both 2-D and 3-D inversions were conducted, and a joint interpretation was made on the basis of these two types of resistivity model.

(2) Beneath the Qaidam Basin, conductor C1 + C2 is interpreted as a ductile layer in the lower crust and upper mantle. This may act as a weak layer, either associated with crustal flow, or as a detachment layer.

(3) The large-scale south-dipping conductor (C4) beneath the ATR is interpreted as a zone rich in aqueous fluids that generated by prograde metamorphic reactions associated with oblique underthrusting of the Tarim Block. These fluids migrate upward through the ATF system and result in serpentinization.

(4) Combining the interpretations above, a geodynamic model is proposed that suggests the rigid block model and continuum model are reconcilable for this study region with the continuum model dominant as evidenced by large scale conductors associated with crustal thickening over a broad region on each side of the ATF.

Acknowledgements

This work was supported by grants from National Natural Science Foundation of China (40974058, 40904025, 41404060), Fundamental Research Funds for the Central Universities (2652014016), China Scholarship Council (2010640041), United States National Science Foundation, Science Foundation Ireland (award 08/RFP/GEO1693 to A.G.J.), and Natural Sciences and Engineering Research Council of Canada Discovery Grant to M.J.U. Thanks to Prof. Larry Brown for his leadership of INDEPTH project, and our field crew for their hard work during the field campaign. Prof. Eric Cowgill and another anonymous reviewer gave detailed comments on the original manuscript, their constructive suggestions are highly appreciated.

Appendix A. Supplementary material

Supplementary material related to this article can be found online at http://dx.doi.org/10.1016/j.epsl.2015.01.025. These data include the Google map of the most important areas described in this article.

References

Avouac, J.-P., Tapponnier, P., 1993. Kinematic model of active deformation in central Asia. Geophys. Res. Lett. 20, 895–898. http://dx.doi.org/10.1029/93GL00128.

Bai, D., Unsworth, M.J., Meju, M.A., Ma, X., Teng, J., Kong, X., Sun, Y., Sun, J., Wang, L., Jiang, C., Zhao, C., Xiao, P., Liu, M., 2010. Crustal deformation of the eastern Tibetan Plateau revealed by magnetotelluric imaging. Nat. Geosci. 3, 358–362. http://dx.doi.org/10.1038/ngeo830.

Becken, M., Ritter, O., Burkhardt, H., 2008. Mode separation of magnetotelluric responses in three-dimensional environments. Geophys. J. Int. 172, 67–86. http://dx.doi.org/10.1111/j.1365-246X.2007.03612.x.

Becken, M., Ritter, O., Bedrosian, P.A., Weckmann, U., 2011. Correlation between deep fluids, tremor and creep along the central San Andreas fault. Nature 480, 87–90. http://dx.doi.org/10.1038/nature10609.

Bedrosian, P.A., Unsworth, M.J., Wang, F., 2001. Structure of the Altyn Tagh Fault and Daxue Shan from magnetotelluric surveys: implications for faulting associated with the rise of the Tibetan Plateau. Tectonics 20, 474–486. http://dx.doi.org/10.1029/2000tc001215.

Bendick, R., Bilham, R., Freymueller, J., Larson, K., Yin, G., 2000. Geodetic evidence for a low slip rate in the Altyn Tagh fault system. Nature 404, 69–72. http://dx.doi.org/10.1038/35003555.

Bertrand, E., Unsworth, M., Chiang, C.-W., Chen, C.-S., Chen, C.-C., Wu, F., Türkoğlu, E., Hsu, H.-L., Hill, G., 2009. Magnetotelluric evidence for thick-skinned tectonics in central Taiwan. Geology 37, 711–714. http://dx.doi.org/10.1130/g25755a.1.

Booker, J., 2014. The magnetotelluric phase tensor: a critical review. Surv. Geophys. 35, 7–40. http://dx.doi.org/10.1007/s10712-013-9234-2.

Burchfiel, B.C., Quidong, D., Molnar, P., Royden, L., Yipeng, W., Peizhen, Z., Weiqi, Z., 1989. Intracrustal detachment within zones of continental deformation. Geology 17, 748–752. http://dx.doi.org/10.1130/0091-7613(1989)017<0448:idwzoc>2.3.co;2.

Calais, E., Dong, L., Wang, M., Shen, Z., Vergnolle, M., 2006. Continental deformation in Asia from a combined GPS solution. Geophys. Res. Lett. 33, L24319. http://dx.doi.org/10.1029/2006GL028433.

Caldwell, T.G., Bibby, H.M., Brown, C., 2004. The magnetotelluric phase tensor. Geophys. J. Int. 158, 457–469. http://dx.doi.org/10.1111/j.1365-246X.2004.02281.x.

Chen, Z., Burchfiel, B.C., Liu, Y., King, R.W., Royden, L.H., Tang, W., Wang, E., Zhao, J., Zhang, X., 2000. Global positioning system measurements from eastern Tibet and their implications for India/Eurasia intercontinental deformation. J. Geophys. Res. 105, 16215–16227. http://dx.doi.org/10.1029/2000jb900092.

Chen, X., Yin, A., Gehrels, G.E., Cowgill, E.S., Grove, M., Harrison, T.M., Wang, X.-F., 2003. Two phases of Mesozoic north–south extension in the eastern Altyn Tagh range, northern Tibetan Plateau. Tectonics 22, 1053. http://dx.doi.org/10.1029/2001tc001336.

Clark, M.K., Royden, L.H., 2000. Topographic ooze: building the eastern margin of Tibet by lower crustal flow. Geology 28, 703–706. http://dx.doi.org/10.1130/0091-7613(2000)28<703:tobtem>2.0.co;2.

Cowgill, E., Yin, A., Feng, W.X., Qing, Z., 2000. Is the North Altyn fault part of a strike-slip duplex along the Altyn Tagh fault system? Geology 28, 255–258. http://dx.doi.org/10.1130/0091-7613(2000)28<255:itnafp>2.0.co;2.

Cowgill, E., Yin, A., Harrison, T.M., Xiao-Feng, W., 2003. Reconstruction of the Altyn Tagh fault based on U–Pb geochronology: role of back thrusts, mantle sutures, and heterogeneous crustal strength in forming the Tibetan Plateau. J. Geophys. Res. 108, 2346. http://dx.doi.org/10.1029/2002jb002080.

Cowgill, E., Yin, A., Arrowsmith, J.R., Feng, W.X., Shuanhong, Z., 2004. The Akato Tagh bend along the Altyn Tagh fault, northwest Tibet 1: smoothing by vertical-axis rotation and the effect of topographic stresses on bend-flanking faults. Bull. Geol. Soc. Am. 116, 1423–1442. http://dx.doi.org/10.1130/b25359.1.

Cowgill, E., Gold, R.D., Xuanhua, C., Xiao-Feng, W., Arrowsmith, J.R., Southon, J., 2009. Low Quaternary slip rate reconciles geodetic and geologic rates along the Altyn Tagh fault, northwestern Tibet. Geology 37, 647–650. http://dx.doi.org/10.1130/g25623a.1.

Darby, B.J., Ritts, B.D., Yue, Y., Meng, Q., 2005. Did the Altyn Tagh fault extend beyond the Tibetan Plateau? Earth Planet. Sci. Lett. 240, 425–435. http://dx.doi.org/10.1016/j.epsl.2005.09.011.

Dupont-Nivet, G., Butler, R.F., Yin, A., Chen, X., 2002. Paleomagnetism indicates no Neogene rotation of the Qaidam Basin in northern Tibet during Indo-Asian collision. Geology 30, 263–266. http://dx.doi.org/10.1130/0091-7613(2002)030<0263:pinnro>2.0.co;2.

Egbert, G.D., 1997. Robust multiple-station magnetotelluric data processing. Geophys. J. Int. 130, 475–496. http://dx.doi.org/10.1111/j.1365-246X.1997.tb05663.x.

Elliott, J.R., Biggs, J., Parsons, B., Wright, T.J., 2008. InSAR slip rate determination on the Altyn Tagh Fault, northern Tibet, in the presence of topographically correlated atmospheric delays. Geophys. Res. Lett. 35, L12309. http://dx.doi.org/10.1029/2008gl033659.

England, P., McKenzie, D., 1982. A thin viscous sheet model for continental deformation. Geophys. J. R. Astron. Soc. 70, 295–321. http://dx.doi.org/10.1111/j.1365-246X.1982.tb04969.x.

England, P.C., Houseman, G.A., Osmaston, M.F., Ghosh, S., 1988. The mechanics of the Tibetan Plateau [and discussion]. Philos. Trans. R. Soc. Lond. Ser. A 326, 301–320. http://dx.doi.org/10.1098/rsta.1988.0089.

Evans, B.W., Hattori, K., Baronnet, A., 2013. Serpentinite: what, why, where? Elements 9, 99–106. http://dx.doi.org/10.2113/gselements.9.2.99.

Gilotti, J.A., 2013. The realm of ultrahigh-pressure metamorphism. Elements 9, 255–260. http://dx.doi.org/10.2113/gselements.9.4.255.

Gold, R.D., Cowgill, E., Arrowsmith, J.R., Chen, X., Sharp, W.D., Cooper, K.M., Wang, X.-F., 2011. Faulted terrace risers place new constraints on the late Quaternary slip rate for the central Altyn Tagh fault, northwest Tibet. Bull. Geol. Soc. Am. 123, 958–978.

Guo, X., Yoshino, T., Katayama, I., 2011. Electrical conductivity anisotropy of deformed talc rocks and serpentinites at 3 GPa. Phys. Earth Planet. Inter. 188, 69–81. http://dx.doi.org/10.1016/j.pepi.2011.06.012.

Hansen, P., 1992. Analysis of discrete ill-posed problems by means of the L-curve. SIAM Rev. 34, 561–580. http://dx.doi.org/10.1137/1034115.

Hansen, P., O'Leary, D., 1993. The use of the L-curve in the regularization of discrete ill-posed problems. SIAM J. Sci. Comput. 14, 1487–1503. http://dx.doi.org/10.1137/0914086.

He, J., Vernant, P., Chéry, J., Wang, W., Lu, S., Ku, W., Xia, W., Bilham, R., 2013. Nailing down the slip rate of the Altyn Tagh fault. Geophys. Res. Lett. 40. http://dx.doi.org/10.1002/2013GL057497.

Herquel, G., Tapponnier, P., Wittlinger, G., Mei, J., Danian, S., 1999. Teleseismic Shear wave splitting and lithospheric anisotropy beneath and across the Altyn Tagh Fault. Geophys. Res. Lett. 26, 3225–3228. http://dx.doi.org/10.1029/1999gl005387.

Hyndman, R.D., Peacock, S.M., 2003. Serpentinization of the forearc mantle. Earth Planet. Sci. Lett. 212, 417–432. http://dx.doi.org/10.1016/S0012-821X(03)00263-2.

Jiang, X., Jin, Y., McNutt, M.K., 2004. Lithospheric deformation beneath the Altyn Tagh and West Kunlun faults from recent gravity surveys. J. Geophys. Res. 109, B05406. http://dx.doi.org/10.1029/2003jb002444.

Jones, A., 1983. The problem of current channeling: a critical review. Geophys. Surv. 6, 79–122. http://dx.doi.org/10.1007/BF01453996.

Jones, A.G., Jödicke, H., 1984. Magnetotelluric transfer function estimation improvement by a coherence-based rejection technique. In: SEG Technical Program Expanded Abstracts, 1984, pp. 51–55. http://dx.doi.org/10.1190/1.1894081.

Karplus, M.S., Zhao, W., Klemperer, S.L., Wu, Z., Mechie, J., Shi, D., Brown, L.D., Chen, C., 2011. Injection of Tibetan crust beneath the south Qaidam Basin: evidence from INDEPTH IV wide-angle seismic data. J. Geophys. Res. 116, B07301. http://dx.doi.org/10.1029/2010jb007911.

Kawano, S., Yoshino, T., Katayama, I., 2012. Electrical conductivity of magnetite-bearing serpentinite during shear deformation. Geophys. Res. Lett. 39, L20313. http://dx.doi.org/10.1029/2012GL053652.

Le Pape, F., Jones, A.G., Vozar, J., Wenbo, W., 2012. Penetration of crustal melt beyond the Kunlun Fault into northern Tibet. Nat. Geosci. 5, 330–335. http://dx.doi.org/10.1038/ngeo1449.

Leloup, P.H., Ricard, Y., Battaglia, J., Lacassin, R., 1999. Shear heating in continental strike-slip shear zones: model and field examples. Geophys. J. Int. 136, 19–40. http://dx.doi.org/10.1046/j.1365-246X.1999.00683.x.

Lévêque, J.-J., Masson, F., 1999. From ACH tomographic models to absolute velocity models. Geophys. J. Int. 137, 621–629. http://dx.doi.org/10.1046/j.1365-246x.1999.00808.x.

Li, S., Unsworth, M.J., Booker, J.R., Wei, W., Tan, H., Jones, A.G., 2003. Partial melt or aqueous fluid in the mid-crust of Southern Tibet? Constraints from INDEPTH magnetotelluric data. Geophys. J. Int. 153, 289–304. http://dx.doi.org/10.1046/j.1365-246X.2003.01850.x.

Liou, J.G., Ernst, W.G., Song, S.G., Jahn, B.M., 2009. Tectonics and HP–UHP metamorphism of northern Tibet – preface. J. Asian Earth Sci. 35, 191–198. http://dx.doi.org/10.1016/j.jseaes.2009.03.001.

Liu, L., Wang, C., Chen, D., Zhang, A., Liou, J.G., 2009. Petrology and geochronology of HP–UHP rocks from the South Altyn Tagh, northwestern China. J. Asian Earth Sci. 35, 232–244. http://dx.doi.org/10.1016/j.jseaes.2008.10.007.

Liu, L., Wang, C., Cao, Y.-T., Chen, D.-L., Kang, L., Yang, W.-Q., Zhu, X.-H., 2012. Geochronology of multi-stage metamorphic events: constraints on episodic zircon growth from the UHP eclogite in the South Altyn, NW China. Lithos 136–139, 10–26. http://dx.doi.org/10.1016/j.lithos.2011.09.014.

McDermott, J., Wu, L., Cowgill, E., 2014. Investigating Cenozoic deformation in the Southeast Tarim Basin using seismic reflection: evidence against large scale thrusting along the northwest Tibetan Margin. AGU Fall Meeting Abstracts.

McNeice, G.W., Jones, A.G., 2001. Multisite, multifrequency tensor decomposition of magnetotelluric data. Geophysics 66, 158–173. http://dx.doi.org/10.1190/1.1444891.

Meade, B.J., 2007. Present-day kinematics at the India–Asia collision zone. Geology 35, 81–84. http://dx.doi.org/10.1130/g22924a.1.

Mériaux, A.S., Ryerson, F.J., Tapponnier, P., Van der Woerd, J., Finkel, R.C., Xu, X., Xu, Z., Caffee, M.W., 2004. Rapid slip along the central Altyn Tagh Fault: morphochronologic evidence from Cherchen He and Sulamu Tagh. J. Geophys. Res., Solid Earth 109, B06401. http://dx.doi.org/10.1029/2003JB002558.

Mériaux, A.S., Tapponnier, P., Ryerson, F.J., Xiwei, X., King, G., Van der Woerd, J., Finkel, R.C., Haibing, L., Caffee, M.W., Zhiqin, X., Wenbin, C., 2005. The Aksay segment of the northern Altyn Tagh fault: tectonic geomorphology, landscape evolution, and Holocene slip rate. J. Geophys. Res., Solid Earth 110, B04404. http://dx.doi.org/10.1029/2004JB003210.

Mériaux, A.S., Van der Woerd, J., Tapponnier, P., Ryerson, F.J., Finkel, R.C., Lasserre, C., Xu, X., 2012. The Pingding segment of the Altyn Tagh Fault (91°E): holocene slip-rate determination from cosmogenic radionuclide dating of offset fluvial terraces. J. Geophys. Res., Solid Earth 117, B09406. http://dx.doi.org/10.1029/2012JB009289.

Meyer, B., Tapponnier, P., Gaudemer, Y., Peltzer, G., Shunmin, G., Zhitai, C., 1996. Rate of left-lateral movement along the easternmost segment of the Altyn Tagh fault, east of 96°E (China). Geophys. J. Int. 124, 29–44. http://dx.doi.org/10.1111/j.1365-246X.1996.tb06350.x.

Molnar, P., Burchfiel, B.C., K'uangyi, L., Ziyun, Z., 1987. Geomorphic evidence for active faulting in the Altyn Tagh and northern Tibet and qualitative estimates of its contribution to the convergence of India and Eurasia. Geology 15, 249–253. http://dx.doi.org/10.1130/0091-7613(1987)15<249:gefafi>2.0.co;2.

Moore, D.E., Rymer, M.J., 2007. Talc-bearing serpentinite and the creeping section of the San Andreas fault. Nature 448, 795–797. http://dx.doi.org/10.1038/nature06064.

Nelson, K.D., Zhao, W., Brown, L.D., Kuo, J., Che, J., Liu, X., Klemperer, S.L., Makovsky, Y., Meissner, R., Mechie, J., Kind, R., Wenzel, F., Ni, J., Nabelek, J., Leshou, C., Tan, H., Wei, W., Jones, A.G., Booker, J., Unsworth, M., Kidd, W.S.F., Hauck, M., Alsdorf, D., Ross, A., Cogan, M., Wu, C., Sandvol, E., Edwards, M., 1996. Partially molten middle crust beneath southern Tibet: synthesis of project INDEPTH results. Science 274, 1684–1688. http://dx.doi.org/10.1126/science.274.5293.1684.

Parkinson, W., 1959. Directions of rapid geomagnetic fluctuations. Geophys. J. R. Astron. Soc. 2, 1–14. http://dx.doi.org/10.1111/j.1365-246X.1959.tb05776.x.

Peltzer, G., Saucier, F., 1996. Present-day kinematics of Asia derived from geologic fault rates. J. Geophys. Res., Solid Earth 101, 27943–27956. http://dx.doi.org/10.1029/96JB02698.

Peltzer, G., Tapponnier, P., 1988. Formation and evolution of strike-slip faults, rifts, and basins during the India–Asia collision: an experimental approach. J. Geophys. Res. 93, 15085–15117. http://dx.doi.org/10.1029/JB093iB12p15085.

Peltzer, G., Tapponnier, P., Armijo, R., 1989. Magnitude of late quaternary left-lateral displacements along the north edge of Tibet. Science 246, 1285–1289. http://dx.doi.org/10.1126/science.246.4935.1285.

Pommier, A., Evans, R.L., Key, K., Tyburczy, J.A., Mackwell, S., Elsenbeck, J., 2013. Prediction of silicate melt viscosity from electrical conductivity: a model and its geophysical implications. Geochem. Geophys. Geosyst. 14, 1685–1692. http://dx.doi.org/10.1002/ggge.20103.

Rao, C.K., Jones, A.G., Moorkamp, M., Weckmann, U., 2014. Implications for the lithospheric geometry of the Iapetus suture beneath Ireland based on electrical resistivity models from deep-probing magnetotellurics. Geophys. J. Int. 198, 737–759. http://dx.doi.org/10.1093/gji/ggu136.

Reynard, B., Mibe, K., de Moortèle, B.V., 2011. Electrical conductivity of the serpentinised mantle and fluid flow in subduction zones. Earth Planet. Sci. Lett. 307, 387–394. http://dx.doi.org/10.1016/j.epsl.2011.05.013.

Rippe, D., Unsworth, M., 2010. Quantifying crustal flow in Tibet with magnetotelluric data. Phys. Earth Planet. Inter. 179, 107–121. http://dx.doi.org/10.1016/j.pepi.2010.01.009.

Ritts, B.D., Biffi, U., 2000. Magnitude of post-Middle Jurassic (Bajocian) displacement on the central Altyn Tagh fault system, northwest China. Bull. Geol. Soc. Am. 112, 61–74. http://dx.doi.org/10.1130/0016-7606(2000)112<61:mopjbd>2.0.co;2.

Rodi, W., Mackie, R.L., 2001. Nonlinear conjugate gradients algorithm for 2-D magnetotelluric inversion. Geophysics 66, 174–187. http://dx.doi.org/10.1190/1.1444893.

Royden, L.H., Burchfiel, B.C., King, R.W., Wang, E., Chen, Z., Shen, F., Liu, Y., 1997. Surface deformation and lower crustal flow in eastern Tibet. Science 276, 788–790. http://dx.doi.org/10.1126/science.276.5313.788.

Shen, F., Royden, L.H., Burchfiel, B.C., 2001a. Large-scale crustal deformation of the Tibetan Plateau. J. Geophys. Res. 106, 6793–6816. http://dx.doi.org/10.1029/2000jb900389.

Shen, Z.-K., Wang, M., Li, Y., Jackson, D.D., Yin, A., Dong, D., Fang, P., 2001b. Crustal deformation along the Altyn Tagh fault system, western China, from GPS. J. Geophys. Res. 106, 30607–30621. http://dx.doi.org/10.1029/2001jb000349.

Siripunvaraporn, W., Egbert, G., 2009. WSINV3DMT: vertical magnetic field transfer function inversion and parallel implementation. Phys. Earth Planet. Inter. 173, 317–329. http://dx.doi.org/10.1016/j.pepi.2009.01.013.

Siripunvaraporn, W., Egbert, G., Lenbury, Y., Uyeshima, M., 2005a. Three-dimensional magnetotelluric inversion: data-space method. Phys. Earth Planet. Inter. 150, 3–14. http://dx.doi.org/10.1016/j.pepi.2004.08.023.

Siripunvaraporn, W., Egbert, G., Uyeshima, M., 2005b. Interpretation of two-dimensional magnetotelluric profile data with three-dimensional inversion: synthetic examples. Geophys. J. Int. 160, 804–814. http://dx.doi.org/10.1111/j.1365-246X.2005.02527.x.

Sobel, E.R., Arnaud, N., 1999. A possible middle Paleozoic suture in the Altyn Tagh, NW China. Tectonics 18, 64–74. http://dx.doi.org/10.1029/1998TC900023.

Styron, R., Taylor, M., Okoronkwo, K., 2010. Database of active structures from the Indo-Asian collision. Eos Trans. AGU 91, 181–182. http://dx.doi.org/10.1029/2010EO200001.

Tapponnier, P., Molnar, P., 1976. Slip-line field theory and large-scale continental tectonics. Nature 264, 319–324. http://dx.doi.org/10.1038/264319a0.

Tapponnier, P., Zhiqin, X., Roger, F., Meyer, B., Arnaud, N., Wittlinger, G., Jingsui, Y., 2001. Oblique stepwise rise and growth of the Tibet Plateau. Science 294, 1671–1677. http://dx.doi.org/10.1126/science.105978.

Thatcher, W., 2007. Microplate model for the present-day deformation of Tibet. J. Geophys. Res., Solid Earth 112, B01401. http://dx.doi.org/10.1029/2005JB004244.

Tilmann, F., Ni, J., Team, I.I.S., 2003. Seismic imaging of the downwelling Indian lithosphere beneath Central Tibet. Science 300, 1424–1427. http://dx.org.doi/10.1126/science.1082777.

Türkoğlu, E., Unsworth, M., Bulut, F., Çağlar, İ., 2015. Crustal structure of the North Anatolian and East Anatolian Fault Systems from magnetotelluric data. Phys. Earth Planet. Inter. In press. http://dx.doi.org/10.1016/j.pepi.2015.01.003.

Unsworth, M., Bedrosian, P.A., 2004. Electrical resistivity structure at the SAFOD site from magnetotelluric exploration. Geophys. Res. Lett. 31, L12S05. http://dx.doi.org/10.1029/2003gl019405.

Unsworth, M., Wenbo, W., Jones, A.G., Li, S., Bedrosian, P., Booker, J., Sheng, J., Ming, D., Handong, T., 2004. Crustal and upper mantle structure of northern Tibet imaged with magnetotelluric data. J. Geophys. Res., Solid Earth 109, B02403. http://dx.doi.org/10.1029/2002JB002305.

Unsworth, M., Jones, A.G., Wei, W., Marquis, G., Gokarn, S.G., Spratt, J.E., 2005. Crustal rheology of the Himalaya and Southern Tibet inferred from magnetotelluric data. Nature 438, 78–81. http://dx.doi.org/10.1038/nature04154.

Varentsov, I.M., Sokolova, E.Y., Martanus, E., Nalivaiko, K., BEAR Working Group, 2003. System of electromagnetic field transfer operators for the BEAR array of simultaneous soundings: methods and results. Izv. Phys. Solid Earth 39, 118–148.

Wallace, K., Yin, G., Bilham, R., 2004. Inescapable slow slip on the Altyn Tagh fault. Geophys. Res. Lett. 31, L09613. http://dx.doi.org/10.1029/2004gl019724.

Wannamaker, P., Hohmann, G., Ward, S., 1984. Magnetotelluric responses of three-dimensional bodies in layered earths. Geophysics 49, 1517–1533. http://dx.doi.org/10.1190/1.1441777.

Wannamaker, P.E., Jiracek, G.R., Stodt, J.A., Caldwell, T.G., Gonzalez, V.M., McKnight, J.D., Porter, A.D., 2002. Fluid generation and pathways beneath an active compressional orogen, the New Zealand Southern Alps, inferred from magnetotelluric data. J. Geophys. Res. 107, 2117. http://dx.doi.org/10.1029/2001jb000186.

Washburn, Z., Arrowsmith, J.R., Forman, S.L., Cowgill, E., Xiaofeng, W., Yueqiao, Z., Zhengle, C., 2001. Late Holocene earthquake history of the central Altyn Tagh fault, China. Geology 29, 1051–1054. http://dx.doi.org/10.1130/0091-7613(2001)029<1051:lhehot>2.0.co;2.

Washburn, Z., Arrowsmith, J.R., Dupont-Nivet, G., Wang, X.F., Zhang, Y.Q., Chen, Z., 2003. Paleoseismology of the Xorxol segment of the central Altyn Tagh fault, Xinjiang, China. Ann. Geophys. 46, 1015–1034.

Wei, W., Unsworth, M., Jones, A., Booker, J., Tan, H., Nelson, D., Chen, L., Li, S., Solon, K., Bedrosian, P., Jin, S., Deng, M., Ledo, J., Kay, D., Roberts, B., 2001. Detection of widespread fluids in the Tibetan crust by magnetotelluric studies. Science 292, 716–719. http://dx.doi.org/10.1126/science.1010580.

Wei, W., Le Pape, F., Jones, A.G., Vozar, J., Dong, H., Unsworth, M.J., Jin, S., Ye, G., Jing, J., Zhang, L., Xie, C., 2014. Northward channel flow in northern Tibet revealed from 3D magnetotelluric modelling. Phys. Earth Planet. Inter. 235, 13–24. http://dx.doi.org/10.1016/j.pepi.2014.07.004.

Wessel, P., Smith, W.H.F., 1995. New version of the generic mapping tools released. Eos Trans. AGU 76, 329. http://dx.doi.org/10.1029/95EO00198.

Wight, D.E., Bostick, F.X., Smith, H.W., 1977. Real-time Fourier Transformation of Magnetotelluric Data. U.S. Dept. of Energy, Washington, DC.

Wittlinger, G., Tapponnier, P., Poupinet, G., Mei, J., Danian, S., Herquel, G., Masson, F., 1998. Tomographic evidence for localized lithospheric shear along the Altyn Tagh Fault. Science 282, 74–76. http://dx.doi.org/10.1126/science.282.5386.74.

Xiao, Q., Zhao, G., Dong, Z., 2011. Electrical resistivity structure at the northern margin of the Tibetan Plateau and tectonic implications. J. Geophys. Res. 116, B12401. http://dx.doi.org/10.1029/2010jb008163.

Xiao, Q., Zhang, J., Wang, J., Zhao, G., Tang, J., 2012. Electrical resistivity structures between the Northern Qilian Mountains and Beishan Block, NW China, and tectonic implications. Phys. Earth Planet. Inter. 200–201, 92–104. http://dx.doi.org/10.1016/j.pepi.2012.04.008.

Xinjiang Bureau of Geology and Mineral Resources, 1993. Regional geology of Xinjiang Uygur autonomous region. Geological Publishing House, Beijing [in Chinese with English abstract].

Yang, J., Xu, Z., Zhang, J., Chu, C.-Y., Zhang, R., Liou, J.-G., 2001. Tectonic significance of early Paleozoic high-pressure rocks in Altun–Qaidam–Qilian Mountains, northwest China. Mem. Geol. Soc. Amer. 194, 151–170. http://dx.doi.org/10.1130/0-8137-1194-0.151.

Yin, A., Harrison, T.M., 2000. Geologic evolution of the Himalayan–Tibetan orogen. Annu. Rev. Earth Planet. Sci. 28, 211–280. http://dx.doi.org/10.1146/annurev.earth.28.1.211.

Yin, A., Rumelhart, P.E., Butler, R., Cowgill, E., Harrison, T.M., Foster, D.A., Ingersoll, R.V., Qing, Z., Xian-Qiang, Z., Xiao-Feng, W., Hanson, A., Raza, A., 2002. Tectonic history of the Altyn Tagh fault system in northern Tibet inferred from Cenozoic sedimentation. Bull. Geol. Soc. Am. 114, 1257–1295. http://dx.doi.org/10.1130/0016-7606(2002)114<1257:thotat>2.0.co;2.

Yin, A., Dang, Y.-Q., Zhang, M., Chen, X.-H., McRivette, M.W., 2008. Cenozoic tectonic evolution of the Qaidam basin and its surrounding regions (Part 3): structural geology, sedimentation, and regional tectonic reconstruction. Bull. Geol. Soc. Am. 120, 847–876. http://dx.doi.org/10.1130/b26232.1.

Yoshino, T., Noritake, F., 2011. Unstable graphite films on grain boundaries in crustal rocks. Earth Planet. Sci. Lett. 306, 186–192. http://dx.doi.org/10.1016/j.epsl.2011.04.003.

Yue, Y., Ritts, B.D., Hanson, A.D., Graham, S.A., 2004. Sedimentary evidence against large strike-slip translation on the Northern Altyn Tagh fault, NW China. Earth Planet. Sci. Lett. 228, 311–323. http://dx.doi.org/10.1016/j.epsl.2004.10.008.

Zhang, J., Meng, F., Mattinson, C.G., 2007a. Progress, Controversies and Challenge of Studies on South Altyn Tagh-North Qaidam HP/UHP Metamorphic Belt. Geol. J. China Univ. 13, 526–545 [in Chinese with English abstract].

Zhang, P.-Z., Molnar, P., Xu, X., 2007b. Late Quaternary and present-day rates of slip along the Altyn Tagh Fault, northern margin of the Tibetan Plateau. Tectonics 26, TC5010. http://dx.doi.org/10.1029/2006tc002014.

Zhao, J., Mooney, W.D., Zhang, X., Li, Z., Jin, Z., Okaya, N., 2006. Crustal structure across the Altyn Tagh Range at the northern margin of the Tibetan Plateau and tectonic implications. Earth Planet. Sci. Lett. 241, 804–814. http://dx.doi.org/10.1016/j.epsl.2005.11.003.

Zhao, J., Jin, Z., Liu, X., 2010. Geoscience Transect from Baicheng to Da Qaidam, Northwestern China. Science Press, Beijing, China.

Zheng, Y.-F., Xiao, W.-J., Zhao, G., 2013. Introduction to tectonics of China. Gondwana Res. 23, 1189–1206. http://dx.doi.org/10.1016/j.gr.2012.10.001.

Zuza, A.V., Yin, A., 2013. Ductile bookshelf faulting: a new kinematic model for Cenozoic deformation in northern Tibet. In: AGU Fall Meeting Abstracts.